AEROACOUSTIC SIMULATION OF A COMPLETE H145 HELICOPTER IN DESCENT FLIGHT

Ulrich Kowarsch, Constantin Öhrle, Manuel Keßler and Ewald Krämer

Institute of Aerodynamics and Gas Dynamics (IAG), University of Stuttgart
Pfaffenwaldring 21, Stuttgart, 70569, Germany
kowarsch@iag.uni-stuttgart.de

Abstract

In the past years, the aeroacoustic noise emission of a helicopter became one of the most important, but also challenging issues in helicopter development. The blade vortex interaction phenomenon is one of the dominant phenomena characterizing the helicopter's aeroacoustic footprint, which is insufficiently predicted by low fidelity computational methods. For a high fidelity noise prediction of a helicopter configuration, a multidisciplinary CFD-CSD-CAA tool chain has been established at the Institute of Aerodynamics and Gas Dynamics of the University of Stuttgart. With higher order CFD computed noise generation at the near field and the noise convection using a Ffowcs-Williams Hawkings based CAA code, very good agreement to measured aeroacoustic noise in wind tunnel as well as free flight experiments of helicopters is achieved. However, the simulations had been limited to the main rotor's geometry up to now, where some residual deviations to the experiment still exist. In this paper, we present a high fidelity aeroacoustic simulation of a complete helicopter configuration and the benefit compared to an isolated rotor simulation in predicting its aeroacoustic noise emission. Shading and reflection effects are clearly resolved, influencing the behaviour of the helicopter's noise radiation. The simulated aeroacoustic noise emission of the helicopter lies within the experimental variation and shows therefore highly promising results for the next generation of aeroacoustic noise prediction.

1 NOTATION

BVI	blade vortex interaction
BPF	blade passing frequency
c_l	sectional lift coefficient
CAA	Computational Aero-Acoustics
CFD	Computational Fluid Dynamics
CSD	Computational Structure Dynamics
DOF	degrees of freedom
EPNL	Effective Perceived Noise Level
GP	ground plate
MR	main rotor
PNLT	tone corrected Perceived Noise Level
R	rotor radius
r/R	relative blade radial station
RMS	root mean square
L	Sound Pressure Level
TR	tail rotor
WENO	Weighted Essentially Non-Oscillatory Scheme
WVL	Wavelet Transformation

2 INTRODUCTION

Helicopters often show the most annoying noise characteristics in decent flight. Strong impulsive noise caused by interactions of vortices with the rotor blades, known as blade vortex interaction (BVI) phenomenon, accounts for increased noise levels in this flight state. Current research is focused on a reliable computational prediction of the aeroacoustic behaviour of the rotor in this flight state. In recent years a growing environmental awareness in society can be observed and therefore more and more attention has been drawn to low noise concepts for instance. To achieve an increased acceptance of helicopters in society, reduced noise levels and therefore an improved aeroacoustic predictive capability in the helicopter design phase are necessary. Limited computational resources and too high numerical dissipation of the vortex structures previously prevented the successful prediction of this phenomenon using CFD methods. Recently, besides the availability of higher computational resources, numerics have made progress in the field of higher order methods to improve the vortex conservation. Investigations of Boyd[1] and Ahmed[2] already presented the advantage using such numerical methods for helicopter simulations in this flight state. Boyd showed that CFD codes using higher order methods are in principle capable of resolving BVI measured in a wind tunnel experiment. A previous joint work between the Institute of Aerodynamics and Gas Dynamics (IAG) of the University of Stuttgart and Airbus Helicopters Deutschland GmbH[3] showed the advantage of using higher order methods to resolve the aeroacoustic noise emission for a full scale free-flight CFD simulation. Comparisons with experimental data confirmed the significant improvement resolving BVI phenomena more reliably than former low order simulations. However, the usual simulation approach to consider only the isolated main rotor geometry for the CFD investigation still showed slight deviations to flight test measurements. Within the present investigation the concept is pushed forward and the full helicopter geometry, including fuselage, skids and tail rotor, is considered. The aim is to resolve the influence of these components to the aeroacoustic noise emission in terms of shading, diffraction and reflection. As in the previous isolated rotor investigation, a flight test according to the ICAO approach test certification is simulated, from which noise emission measurements are available. The aeroacoustic results are compared to microphone measurements as well as to the results of the isolated rotor simulation.

3 METHODS

3.1 CFD Solver: FLOWer

For the current investigation, the block structured finite volume Reynolds-averaged Navier-Stokes (RANS) CFD code FLOWer of the German Aerospace Center (DLR)[4] is used. The RANS equations are closed using the Wilcox k-ω turbulence model[5] with a fully turbulent flow. The time discretization is achieved by integrating the governing differential equation in space with the implicit dual time-stepping approach according to Jameson[6]. The consideration of relative grid movements using an Arbitrary Lagrangian Eulerian (ALE) approach enables the code for helicopter flow simulation. In addition, the Chimera technique for overset grids simplifies the meshing of complex helicopter geometries like rotor-fuselage configurations including relative grid movements. To consider the effects of fluid-structure interaction on the rotor blade, the mesh is deformed to a given structural deformation of the blade for each time step. The efficiency of the computation is achieved by a multi-block structure of the grid to enable parallel computing.

Within the past years, several important helicopter related features have been implemented into FLOWer by IAG and Airbus Helicopters Deutschland. Within the so-called HELI-version, an automated strong and loose coupling exchange with CSD Tools, a grid deformation algorithm and extensive rotor related post-processing output have been included[7].

In the course of this code improvement cooperation, the CFD solver was extended with different methods of fifth order spatial WENO schemes by IAG[8] to guarantee a detailed conservation of the flow field and especially vortices. First applications of the higher order methods in FLOWer confirmed significant improvements in wake conservation and load prediction in case of wake-structure interactions[9;10]. For the presented simulation, a fifth order WENO-Z scheme according to Borges[11] is used for the convective fluid state reconstruction at cell boundaries. The resulting Riemann problem is solved using the upwind HLLC scheme according to Toro[12]. The viscous fluxes are solved with conventional central differences of second order accuracy.

3.2 CSD: CAMRAD II

Besides a high-fidelity aerodynamic investigations using CFD, an accurate reproduction of the helicopters flight state as well as major structural dynamic characteristics are required. Therefore, the Comprehensive Analytical Model of Rotorcraft Aerodynamics and Dynamics (CAMRAD II) code[13] is integrated into the numerical tool chain. The rotorblade's structural dynamics are modelled by a collection of finite beam segments whose loads can be prescribed by program input. This allows a forwarding of loads from FLOWer to CAMRAD II and the feedback of resulting blade deformations. Coupling CFD and CSD creates a closed loop by exchanging loads and deformation information. For this investigation, the cycle is performed after each rotor revolution by the exchange of periodic loads and deformations. This exchange of periodic rotor characteristics is known as the weak fluid-structure coupling. To achieve a physical flight state, the flight mechanics of the helicopter is taken into account to achieve a force and moment free flight state of the helicopter. Therefore, a free-flight helicopter trim is performed including 6 degrees of freedom (DOF). Beside the 3 main rotor controls, collective and cyclic pitch, the fuselage pitch and roll orientation as well as the tail rotor collective are taken into account. The yaw angle of the helicopter is fixed at zero degree. Analogue to the structural dynamic trim, forwarded periodic CFD loads allows the CSD code to determine the load residuals to be eliminated by DOF angle adaptation.

3.3 CAA: Aeroacoustics

For calculation of noise emission towards the far field, the CAA code ACCO[14], developed by IAG, is applied. The basis for the computation is given by the converged solution of the CFD computation in terms of a data extraction over the time.

ACCO uses the Ffowcs Williams-Hawkings equation

$$
\begin{aligned}
\frac{\overline{\partial}^2 \overline{\rho}'}{\partial t^2} - c^2 \overline{\nabla}^2 \overline{\rho}' = {} & \frac{\partial^2}{\partial x_i \partial x_j} \left[T_{ij} H(f_S) \right] \\
& - \frac{\partial}{\partial x_i} \left[(p' n_i + \rho u_i (u_n - v_n)) \delta(f_S) \right] \\
& + \frac{\partial}{\partial t} \left[(\rho_0 v_n + \rho (u_n - v_n)) \delta(f_S) \right]
\end{aligned} \tag{1}
$$

for acoustic modelling. $\overline{\rho}'$ is the density fluctuation, p' the pressure fluctuation, n_i the normal vector, u_n the normal component of the fluid velocity, v_n the normal component of the surface velocity, δ the Dirac delta function, T_{ij} the Lighthill tensor, and $H(f_S)$ the Heaviside function of the surface function of the integration surfaces $f_S = 0$. With the use of the wave equation on the left hand side, the flow outside of the integration surface is assumed to be an undisturbed freestream. The right hand side of equation (1) represents the source terms, which can be interpreted as volume displacement (monopoles), load fluctuations (dipoles), if the integration surface f_S coincides with the physical surface, and turbulence, shear layers, and compressibility effects (quadrupoles).

4 FLIGHT TEST DESCRIPTION

Main focus of this paper is on the descent flight, as this flight condition often shows the most annoying noise characteristics due to strong impulsive noise. To assess the aeroacoustic predictive capability of the numerical tool chain described before, the simulation results will be compared to flight test data. The considered flight tests were performed in June 2012 within the scope of the noise certification campaign of the H145 helicopter. Figure 1 schematically illustrates the noise certification approach procedure including trajectory constraints. In accordance to the helicopter noise certification rules and regulations[15], the helicopter follows a flight path with a descent angle of 6° at a flight speed of V_y (best rate of climb speed). Besides the center microphone, which is overflown in an altitude of 120 m above ground, two microphones were installed perpendicular to the flight track at a lateral distance of ±150 m.

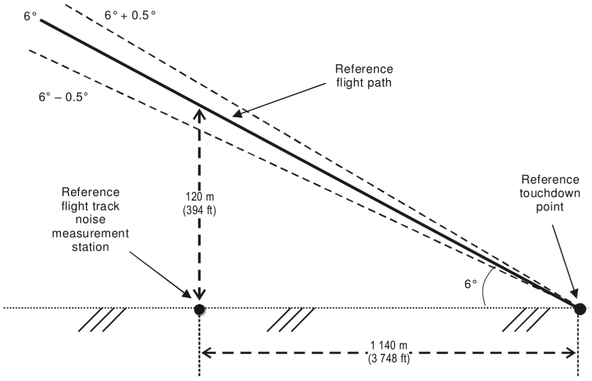

Fig. 1. Flight boundaries for approach test condition[15].

By way of derogation from noise certification for this test case, microphones are considered which were placed above ground plates (cf. Figure 2). In this case, the signal experiences a defined total reflection on the ground plate (GP), which can be considered analogue in the simulation by a doubling of the free-space computed pressure-time signal. Aeroacoustic key values are computed according to the ICAO evaluation procedure. For the evaluation, the microphones signals are considered *as measured* in the form of pressure-time signals. A more detailed description and evaluation of the noise measurement campaign of the H145 gives Reference 15 and 16.

Fig. 2. Installation of considered microphones over a ground plate (GP) for the approach flight.

Table 1 gives an overview of the averaged flight test conditions as well as major figures of the H145 helicopter. The numerical results also consider measured wind data (direction and speed) and atmospheric sound absorption.

Characteristics	
Main rotor blades	4
Main rotor radius	5.5 m
Main rotor freq.	Ω_{MR}
Fenestron® blades (unevenly distributed, symmetric)	10
Fenestron® freq.	Ω_{TR}=8.2 Ω_{MR}
Fenestron® modulation freq.	2 Ω_{TR}
TAS	70 kn
Flight path angle	6.0 °
Height over mic.	120 m
No. of mic.	3

Table 1. Figures of H145 and average flight test condition.

5 SIMULATION

5.1 CFD / CSD

The helicopter geometry considered in the CFD simulation covers all aerodynamically relevant components, including the main rotor with a detailed model of the rotor head, the fuselage including skids and the full Fenestron® anti-torque system with stator and rotor blades. For a more precise simulation of the aft body wake interacting with the Fenestron®, the turbine exhaust is simulated in terms of a boundary condition prescribing the mass flow through the engine and the exhaust temperature. Conservativeness is ensured with a mass coupling between the inlet and outlet surface of each engine. Table 2 shows grid components of the complete helicopter configuration including 59 separate meshes. The body meshes are extruded from $y^+ \approx 1.0$ (on main rotor blades $y^+ \approx 0.5$) with a cell height ratio of 1.15 until the resolution of the Cartesian background mesh is reached. On body mesh boundaries, the exchange of the fluid state is performed using the Chimera technique. The near-field in the off-body mesh has a resolution of 6% of the blade chord length. The coarsening of the off-body mesh towards the far field is enabled by the use of hanging grid nodes. The background mesh is created automatically with a mesh refinement in specified areas of interest. With the focus on aeroacoustic simulation, the area with the finest grid resolution is defined to enable a surface definition around the complete helicopter, which does not have any inflection points. This guarantees an extraction of explicit pressure disturbances used as a CAA integration surface. In addition, the finest grid resolution ensures a wave propagation of the pressure disturbances onto the integration surface with little numerical dissipation. Figure 3 shows an overview of the merged grid components.

Component	No. of blocks	No. of cells (M)
Background	6563	106.3
Main rotor blade	4× 230	4× 6.9
Blade root	4× 56	4× 1.0
Rotor hub system	610	9.2
Fuselage	1505	26.7
Skid system	375	7.1
Fenestron® stator + rotor	670	11.9
Total	**10867**	**191.7**

Table 2. Grid components of complete helicopter CFD setup.

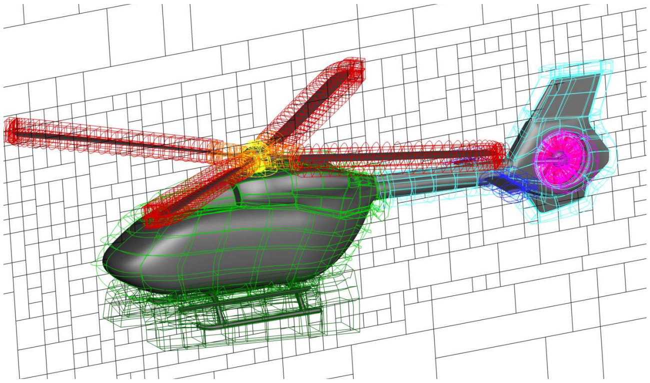

Fig. 3. Merging of grid components to a full helicopter CFD setup using the Chimera technique.

Previous simulations showed sufficient mapping of forces and moments acting on the surface using lower order methods in combination with reasonable grid resolution. Therefore, the simulation is started using the low computational effort 2nd order JST method for the free-flight trim process. The free-flight CFD-CSD trim coupling is performed after 2 computed main rotor revolutions to overcome start-up effects. The stop criterion for the free-flight trim process is set to a residual less than 0.1 $^{m}/_{s^2}$ translational acceleration and 1 $^{\circ}/_{s^2}$ angular acceleration. This process required 12 iterations between the CFD and CSD code to converge to the stop criterion, with up to 1.5 CFD computed main rotor revolutions between each iteration step. The long trim process is mostly a consequence of the fact that the investigated slow descent flight state is highly unsteady due to low power requirement and therefore low required anti-torque thrust. This leads to a high sensitivity and low damping against small disturbances to the tail rotors collective angle adjustment. Table 3 shows the remaining residuals of the accelerations as well as the deviation of the trim objectives from the average values measured in the experiment. Comparing the deviations to the RMS value of the experiment shows that most values lies within the typical fluctuation range of the flight test. The most significant discrepancy is present in the tail rotor collective angle, representing the compensation of the torque moment. Due to the already mentioned low thrust required and the highly detached flow, a deviating estimation in the numerical tool chain is not unexpected.

H/C acceleration residual		$[m/s^2]$
$a_{vertical}$		0.04
$a_{longitudinal}$		-0.08
$a_{lateral}$		-0.01
Trim objective	$\Delta_{CFD-exp}[^\circ]$	RMS of exp.
Control angel		
$\Theta_{0,MR}$	0.52	0.67
$\Theta_{c/lateral}$	0.36	0.20
$\Theta_{s/longitudinal}$	0.90	0.37
$\Theta_{0,TR}$	3.19	0.93
Fuselage orientation		
Θ_{pitch}	0.68	0.67
Φ_{roll}	0.17	2.47

Table 3. Trim objective of 6 DOF free flight trim.

After convergence of the trim process, the simulation is switched to 0.25° azimuthal resolution and 5th order WENO-Z discretization, and continued for 3 more main rotor revolutions to achieve a full higher order spatial flow field with a fine temporal discretization. The switch showed no significant change in forces and moments giving reason for a further CFD-CSD trim iteration.

Mandatory for the consideration of the long time aeroacoustic noise emission is a database with at least one period of a periodically assumed flow field. For a helicopter, this is aimed for the primary noise sources, the main and the tail rotor. In case of the H145 helicopter, the Fenestron® tail rotor system has a 8.2 times higher rotational frequency as the main rotor, leading to a periodicity each 5th main rotor revolution. Thus, the CFD simulation is continued for these 5 main rotor revolutions with comprehensive output for the evaluation and CAA post-processing.

An extensive block splitting of the structured grids enables an efficient parallelization of the simulation. The CFD simulation was performed on the High Performance Computing Center (HLRS) in Stuttgart on the Cray XC40 Hornet system using 6000 cores with ≈700 WENO time steps per 24 hours.

5.2 Aeroacoustic post-processing

As already mentioned, the data used for the aeroacoustic noise emission is extracted from the CFD field solution in each time-step. In this case, 2D integration surfaces for fast pre-processing are chosen. Due to missing volume data provided to CAA with this restriction, a fully developed flow field has to be present to include quadrupole noise. Using the RANS CFD method, quadrupole noise is only produced at shocks or in the shear layer due to the usage of turbulence models in the blade boundary layer. This leads to an integration surface located as far as necessary and as close as possible to the body surface. With the usage of the higher order method it is ensured that only minor numerical dissipation between the noise sources and integration surface is introduced. Figure 4 shows the integration surfaces investigated in this paper. The reference integration surface is presented by the permeable surface around the complete helicopter (green) in a small distance from the body surface. With the location within the finest grid resolution a detailed transport of the pressure disturbances is ensured.

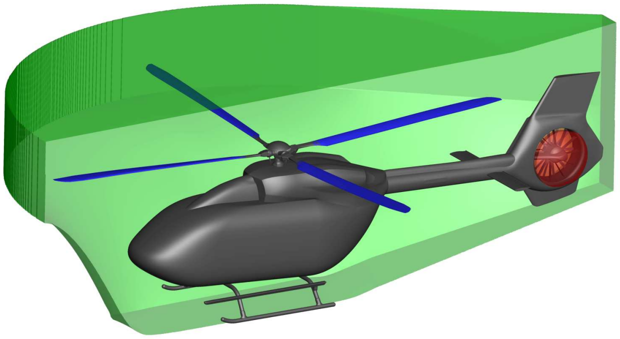

Fig. 4. Location of fluid state extractions used as integration surfaces for the CAA computation.

The primary noise drivers in the considered flight state are lift and load fluctuations (impulsive noise), which are dominated by the main rotor and produced on the physical surface of the rotor. Therefore, an other integration surface is evaluated, which coincides with the physical rotor surface to approximately extract the main rotor proportions of the total signal. With the neglected fuselage pressure signature and negligible reflection feedback from the fuselage, the difference between the integration surface around the complete helicopter (green) and the main rotor blades (blue) reveals the influence in terms of reflection, shading and diffraction effects of the fuselage.

The tail rotor noise is approximately separated by an integration surface closing the shroud of the Fenestron® (red). On each integration surface, the pressure signature is extracted for each CFD time step leading to a sampling frequency of ≈8900 Hz with overall 7200 samples.

With the solution of the Ffowcs Williams-Hawkings equation, time domain acoustic pressure is computed at locations of interest in the far field, which are called observers. Further post-processing of the time domain pressure history leads to aeroacoustic specific values such as narrow-band spectra, Sound Pressure Level (L) and tone corrected Perceived Noise Level (PNLT).

In case of near-field acoustic evaluations, pressure time history at discrete points is directly extracted from the CFD solution.

Wavelet transformation

Resolving the characteristic disturbances of BVI in a pressure time signal with the usually used Fourier transformation lacks a detailed mapping of the temporally restricted events. The character of the non-trigonometrical shaped BVI events leads to undesired leakage effects applying a Fourier transformation. Only a finite frequency range, usually between the 6th-40th BPF, can be assigned to BVI noise. This leads to noise associated to BVI during time spots where no BVI events occur and may be caused by other components in the same frequency range. Therefore, a wavelet transformation is performed to isolate the BVI events of the pressure time signal in order to quantify their contribution to the overall signal. Inspired by the BVI identification proposed by Stephenson and Greenwood[17], the Morlet wavelet is chosen, which adequately characterizes helicopter acoustic signals, especially the impulsive, wavelet shaped BVI events. Applying the wavelet transformation to the pressure time signal $p(t)$ gives the scales of mother wavelets $\tilde{p}(f,t)$ assigned to the investigated frequencies f over the considered time window t. A filter criterion is designed to isolate BVI events which satisfy the condition

$$\tilde{p}_{BVI}(f_i,t_i) = \begin{cases} \tilde{p}(f_i,t_i) & \text{if } E_{BVI}(t_i) > \\ & \quad \alpha_{cut} E_{MR}(t_i \pm t_{rev}) \\ 0 & \text{otherwise} \end{cases} \tag{2}$$

with $E_{BVI}(t_i)$ as the spectral wavelet intensity in decibel of $\tilde{p}(f_i,t_i)$ over a frequency band between 4th-16th BPF, $E_{MR}(t_i \pm t_{rev})$ the spectral intensity in decibel between 1st-4th BPF representing the main rotor's base noise level averaged over one main rotor revolution t_{rev} around the considered time t_i. The scaling factor α_{cut} gives the threshold level for which proportion of the main rotor's base intensity has to be reached to define the occurring wavelet as a BVI event, defined for this investigation to 0.85. In addition, a blending function requires the filter criterion to be satisfied for a time range greater than 5° main rotor azimuth, in order to suppress undesired detected disturbances. After the application of the filter criterion, $\tilde{p}_{BVI}(f,t)$ is transformed back into the time domain and post-processed for instance to identify the BVI contribution to the overall noise emission.

Figure 5 shows the application of the designed filter to a pressure time signal sequence. The BVI events are successfully extracted from the raw pressure time signal and the time windows between the events remain untouched.

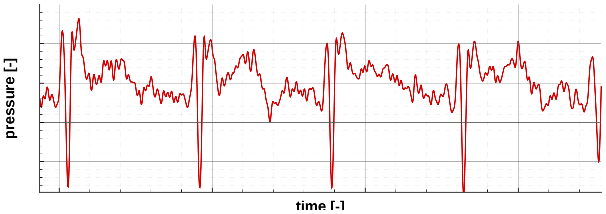

(a) Raw pressure time signal

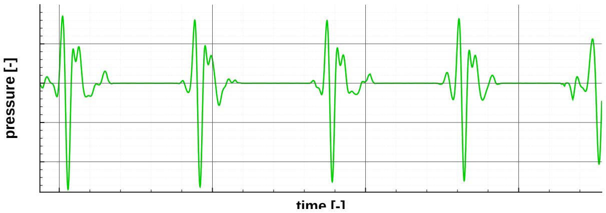

(b) Extracted BVI events

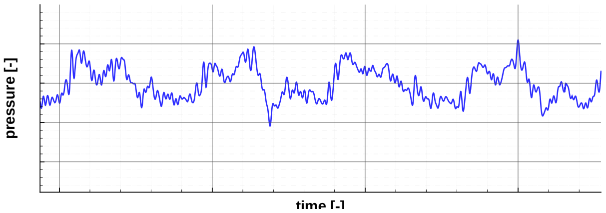

(c) Residual signal without BVI events

Fig. 5. Adaption of the designed wavelet filter to detect BVI events in a pressure time signal.

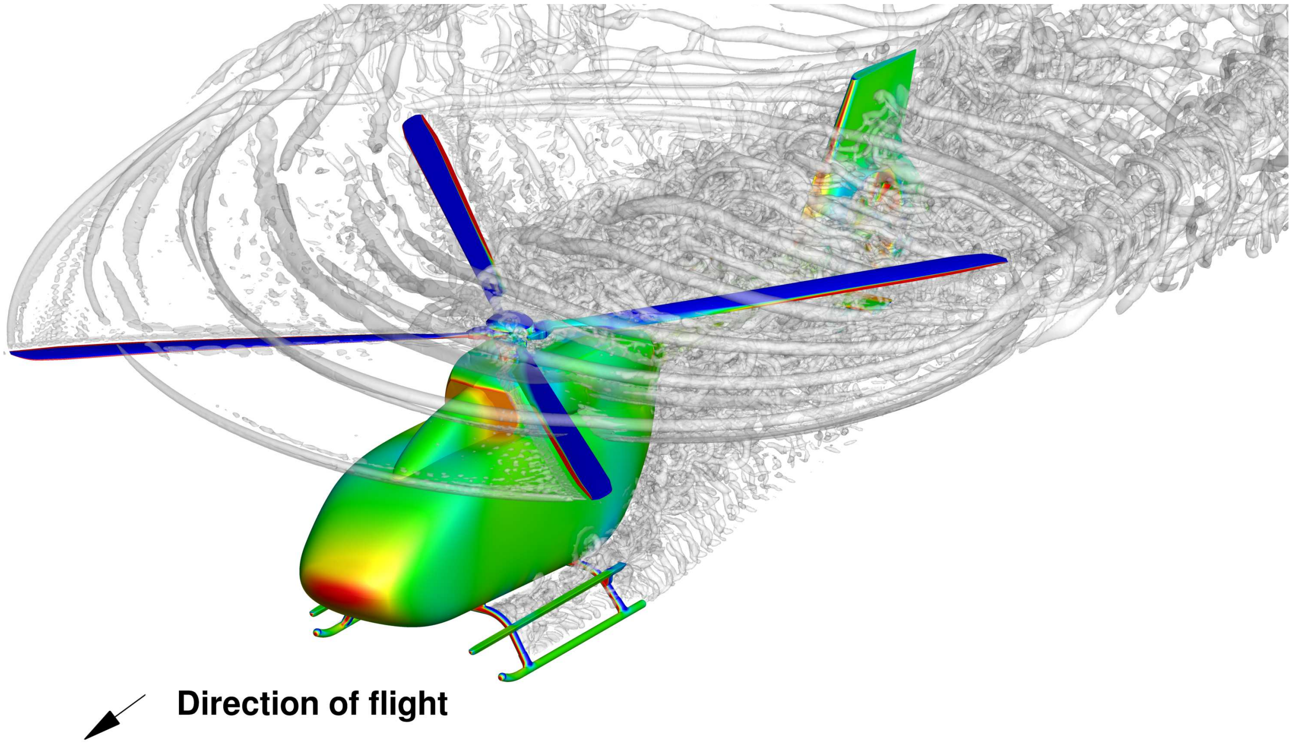

Fig. 6. λ_2-visualization of the flow field around the H145 in a BVI relevant descent flight with the pressure contour on the surface.

6 NUMERICAL RESULTS

6.1 Aerodynamic flow field

The vortex structure of the flow field around the helicopter is shown in Figure 6 using the λ_2-criterion for the vortex visualization. The high grid resolution in the near field area of the helicopter in combination with the higher order WENO-Z method yields a highly detailed resolution of the vortex structure. The blade vortices are preserved compact during their convection downstream, which is a necessary condition for a detailed representation of the blade vortex interactions, clearly notable in the flow field. Moreover, tip vortices sweeping over the subsequent blade cause shear layer roll up effects, which cause secondary vortex structures interacting with the blade as well. This can be seen at the advancing blade side where several non blade tip vortices are present generated by the described phenomenon.

At the engine inlet, the mass flow into the engines is notable with a lower pressure increase compared to the stagnation point at the fuselage front side. In the wake of the skids a typical von Kármán-like vortex street is visible produced by the cylindrically shaped skids.

The highly resolved grid is kept up to the tail fin, from where on a coarsening to the far field is deployed. This is also present in the vortex visualization with a thickening of the vortices as well as strong dissipation of small scale disturbances, and notable in the area behind the fin.

The influence of the engine exhaust is visualized in Figure 7 by slices marking temperature hot spots behind the fuselage. The cooling rate of the high temperature exhaust, prescribed by the boundary condition, is shown within the exhaust jet immediately after the exhaust. Convecting downstream, the jets disintegrate into a turbulent structure due to the high exhaust speed and its shear layer. Moreover, the exhaust interacts with the rotor downwash and the highly turbulent rotor hub wake, increasing the

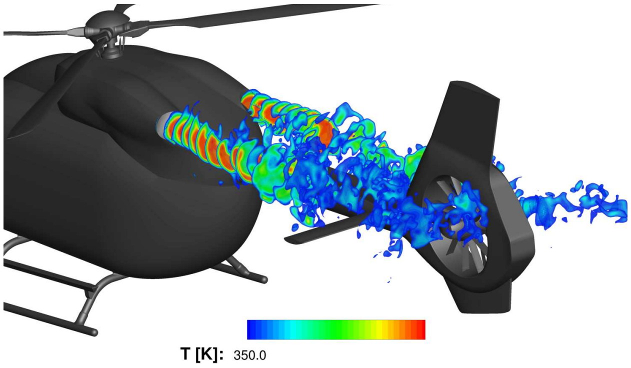

Fig. 7. Engine exhaust visualization by temperature contour.

turbulence. After the mixing taking place in the area of the tail boom, the jet still contains high temperature areas influencing the inflow of the Fenestron® and interacting with the stabilizers.

Figure 8 shows the time averaged normalized density distribution of the Fenestron® inlet. Due to the freestream condition, density reduction is mainly driven by temperature superelevation in the field caused by the engine exhaust wakes. An elliptical area with distortion downstream with reduced density is present at the Fenestron® inlet disc. The interaction with the rotor hub wake and especially the engine wake leads to an efficiency reduction of around 6.1 % due to the reduced inlet density.

Figure 9 shows the different wake structures caused by the helicopter components. The wake areas are identified by the computation of mass-free particles seeded directly downstream to the respective structure component. The particles are injected into the flow field every 5° main rotor azimuth and convected over 3 main rotor revolutions. The final particle situation is taken and compared with a λ_2 vortex isosurface. By an inverse distance weighting, the allocation of the vortex to the respective component wake is determined. The expected vertical distribution is found, whereby blending effects are visible especially between the rotor hub wake and the engine exhaust. A highly turbulent wake structure is present for the fuselage, which indicates strong flow detachment at the fuselage rear. The interaction with the tail rotor is mainly driven by the fuselage, rotor hub and engine wake. The influence of the downwash is mostly seen at the rotor hub wake fading significantly towards the fuselage and skids wake.

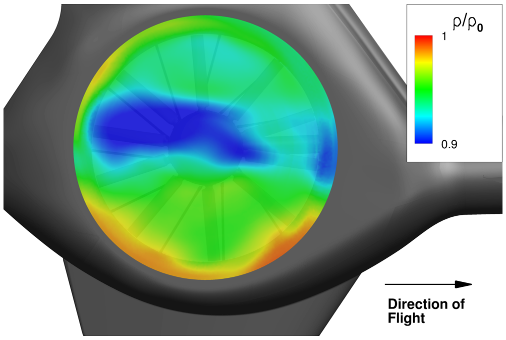

Fig. 8. Time averaged normalized density distribution on Fenestron® inlet.

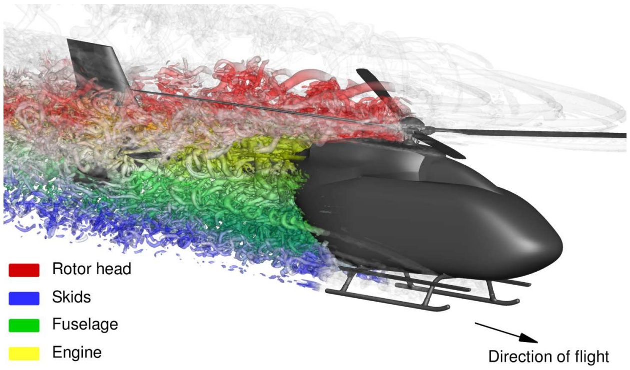

Fig. 9. Delimitations of the wakes caused by different structural component of the helicopter.

Main Rotor Forces

Prior to the investigation of the main rotor forces, the periodicity of the main rotor is to be ascertained. Due to the consideration of the rotor hub geometry, which not necessarily induces rotor harmonic flow disturbances, no intermittency with the main rotors BPF frequency can be expected. The influence of other components like the tail rotor system is expected to be negligible. To resolve the influence of non-MR periodic flow phenomena to the occurring BVI events, a quantification in terms of the RMS lift coefficient over 5 rotor revolutions is depicted in Figure 10. The RMS values show that only non main rotor harmonic fluctuations are found in the rotor hub wake. However, the area of concern investigating the BVI on the rotor disc (30°-330° azimuth) shows a flawless periodicity.

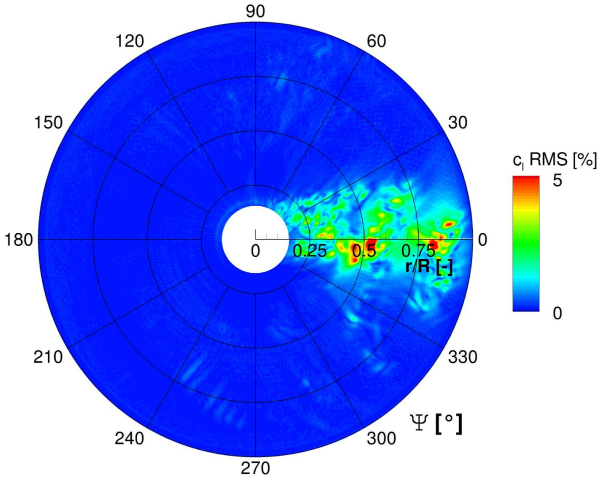

Fig. 10. Percentage portion of the root mean squared sectional lift coefficient c_l computed over 5 rotor revolutions with respect to the mean lift coefficient.

One primary driver for aeroacoustic impulsive noise emission by the rotor is the time rate of load change on the blades. Therefore, the azimuth angle was taken as the independent variable and the azimuthal derivative of the blade load is formed. In Figure 11, the azimuthal derivative of the sectional lift coefficient c_l in polar coordinates is shown. As the underlying data for these calculation, the averaged sectional

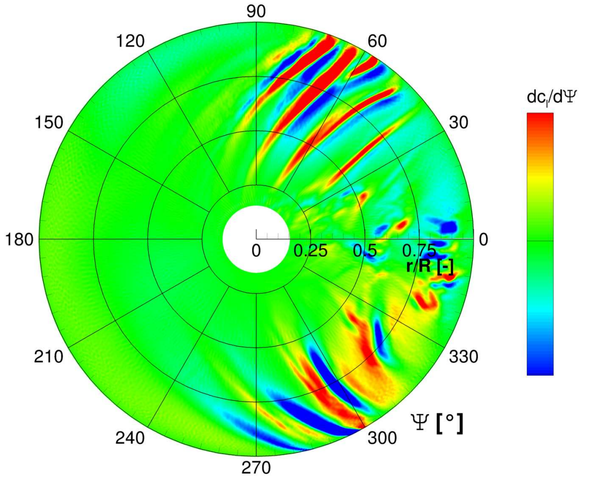

Fig. 11. Azimuthal (time) derivative of the sectional lift coefficient ($c_l/d\Psi$)

lift coefficient over 5 rotor revolutions is taken. BVI events appear as strong short time load fluctuations on the retreating blade side in the range between Ψ=270°-320° as well as on the advancing side between Ψ=30°-90°. Comparing the advancing and the retreating blade side, the superposition of the forward flight speed and the rotation speed characterize the time occurrence of the BVI events. On the advancing blade side, short time, high frequency BVI driven load fluctuations are found, whereas the BVI events on the retreating blade side occur with lower frequency.
Behind the rotor head in the vicinity of Ψ=0° high load gradients are encountered as well. Since the RMS value shows high non-rotor-periodic load fluctuations, non-rotor-harmonic noise is expected to arise in this area.

6.2 Aeroacoustic emission

Aeroacoustic noise of the full helicopter

The impulsive noise emitted by the main rotor is in direct dependency on the load fluctuations shown in Figure 11. However, the most important characteristic for the overall noise emission of the rotor is the spatial distribution and temporal occurrence of the noise sources in addition to their individual strength. The superposition of the emitted acoustic waves shows strong directional dependency due to phase offsets and varying radiation. Figure 12 shows a hemisphere under the helicopter coloured with the computed sound pressure level, based on the integration surface surrounding the complete helicopter. High noise levels are found on the starboard side of the helicopter with a maximum direction upstream-downward. This coincides with the typical radiation direction of the impulsive dipole-shaped noise caused by BVI on the advancing blade side. At the port side a considerably lower noise emission is present with a spot in the downstream area. Beyond the BVI events taking place at the retreating blade side, the high noise level in this area is caused by the Fenestron® tail rotor.

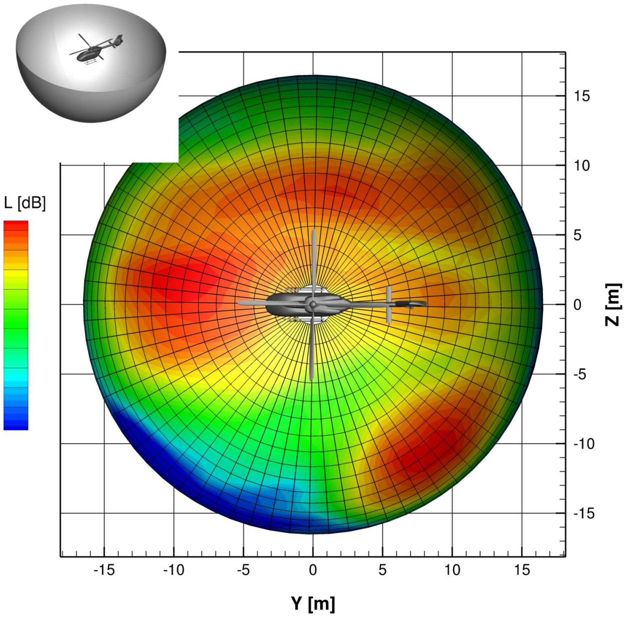

Fig. 12. Aeroacoustic noise footprint of the helicopter on a 3-rotor-radii-hemisphere (integration surface complete helicopter).

BVI radiation

Besides the fundamental noise produced by the main and tail rotor thrust, the BVI events have a high contribution to the helicopter's noise emission. After the discussion of the complete aeroacoustic noise emission, Figure 13 shows the radiation of noise in terms of the Sound Pressure Level, which is assignable to BVI. The isosurface shows the directivity of the high BVI noise areas and the plane shows the BVI related noise footprint 4.5 radii under the helicopter. Comparing the BVI radiation with the overall noise carpet in Figure 12 shows that the local high noise areas coincide with the BVI radiation areas. However, at the starboard side of the helicopter, no BVI assignable noise could be identified in the pressure time signal despite a high sound pressure level found in the overall noise footprint in Figure 12. The occurring noise in this area is mainly driven by the fundamental rotor noise superimposed with tail rotor noise. The strongest BVI noise emission with its radiation marked by the isosurface is found upstream. Tracing back its radiation to the helicopter, the source area is found at the advancing blade side of the main rotor. The slightly non-linear shape of the isosurface towards the far field refers to an influence of the fuselage by reflection and diffraction effects. A further BVI associated noise emission downstream is found with lower strength and expansion. The source for this area is found in the retreating blade side area of the main rotor. The previously discussed coherence of the noise sources is made clear in this visualization as well. The advancing blade side shows a significantly stronger BVI noise radiation compared to the retreating blade side, despite comparable strength and amount of occurring load fluctuation events taking place in the respective quadrant.

Minor wrongly detected BVI areas in the vicinity of the tail rotor are found which are caused by the assumed distance weighting of the computed noise level, whose error increases towards the helicopters proximity.

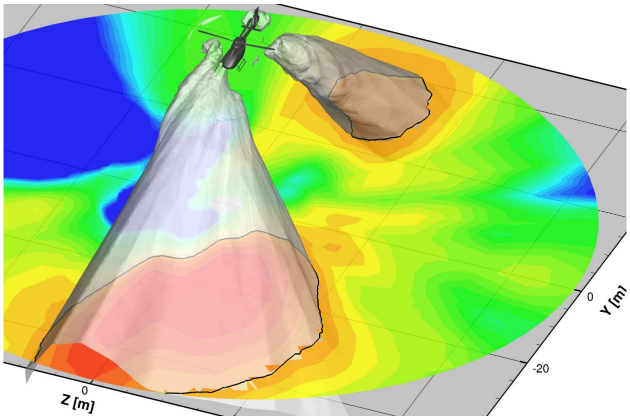

Fig. 13. Radiation of BVI assignable noise emission of the helicopter with a slice 4.5 rotor radii under the helicopter.

Aeroacoustic influence of helicopter components

The different approximated noise emissions of the main helicopter components in terms of main rotor and Fenestron® emission are shown in Figure 14. The carpets are computed on the basis of the integration surfaces close to the respective rotor illustrated in Figure 4. For comparison purposes, the noise emission using the integration surface around the complete helicopter is shown as well. Full helicopter and main rotor blades carpets have the same color scaling, whereas the Fenestron® carpet has an offset (L_{ref} marks the same sound pressure level).

Comparing the main rotor (cf. Figure 14(b)) with the overall noise emission (cf. Figure 14(a)), a reduction in the complete helicopter noise footprint can be found. This is mainly caused by the shading of the fundamental rotor noise by the fuselage components including the tailboom. Besides the reduction of the maximum, the spread of the high noise area (cf. Figure 14(a) marker (1)) is reduced in the vicinity of the helicopter and mostly downstream, whereas

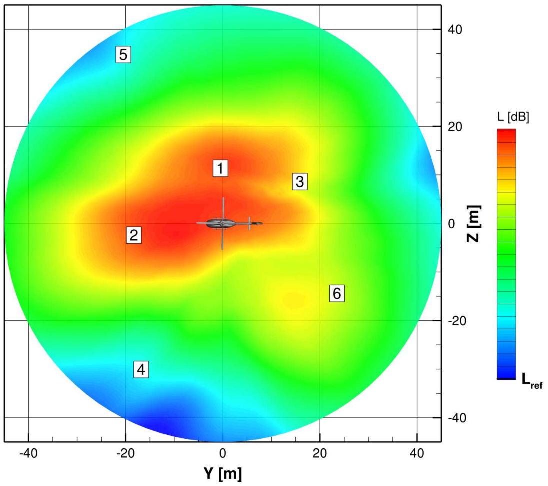

(a) Full helicopter

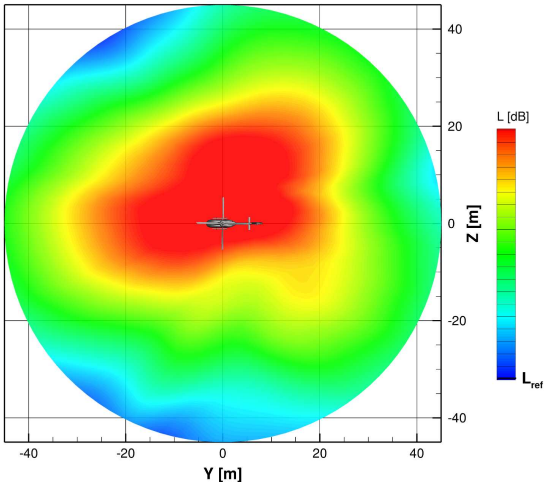

(b) Main rotor blades

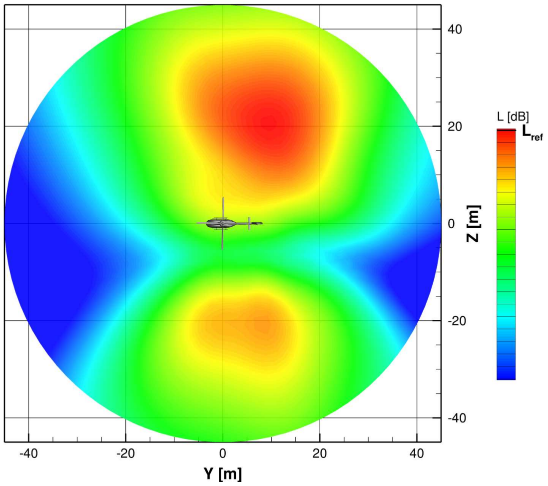

(c) Fenestron®

Fig. 14. Noise emission on a carpet 4.5 rotor radii under the rotor disc coloured with the sound pressure level for different CAA post-processed integration surfaces.

the shape directly in front of the rotor only shows slight differences (2). Notable is the shading by the tailboom in the constriction at the rear with a slight lateral displacement to the starboard (3). Upstream at the port carpet boundary (4), a lower noise level is found compared to the main rotor noise emission, whereas at the upstream starboard carpet boundary (5) the noise increases. This asymmetric influence, approximately unaffected by the tail rotor, indicates explicit influence of the fuselage to directed local noise emission. The influence of the tail rotor noise (cf. Figure 14(c)) causes the overall footprint to remain at higher levels towards the carpet's starboard boundary. At the port side the influence of the tail rotor leads to a local maximum compared to the main rotor noise emission (6).

As the most important influence, the reflection effect of the fuselage is determined on the basis of the CFD extracted pressure time signals on the fuselage surface (cf. Figure 15). A Fourier transformation is performed and the BVI related frequency range between the 6th-16th BPF is considered. To determine the orientation of the reflected pressure waves, the correlation between the spatial phase distribution on the surface for each frequency is considered. A spatial differential operator on each element of the surface is formed, which allows the computation of the incoming pressure wave angle. A sum over the considered frequency range with the wave angles scaled with the respective sound pressure level of the frequency gives the BVI assigned wave angle of incidence on the fuselage surface (blue vectors, averaged over several surface points for illustration purpose). With the surface patch orientation, the reflected wave (orange vectors) is completed. The incoming wave vectors are extended backwards to their intersection point with the rotor disc, at which the temporal load gradient introduced in Figure 11 is depicted. The intersection points with the rotor disc allow a clear assignment of the considered waves to the BVI events of the main rotor blades in the area of 60 ° azimuth. The reflection shows no significant scattering of the waves due to the non-curvature geometry, but rather a constant reflection orientation slightly upstream. At the port side of the fuselage, only highly scattered reflections can be indicated owing to hardly occurring noise reflection.

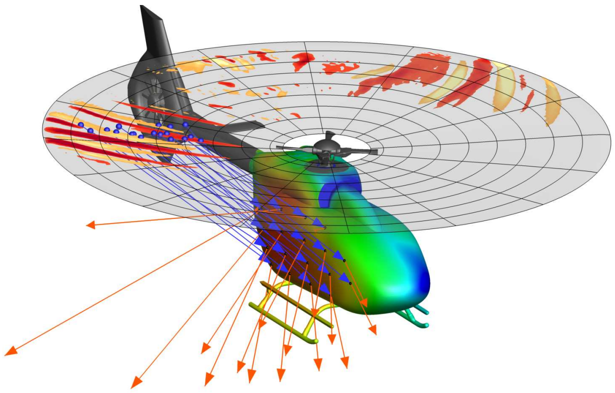

Fig. 15. Computation of the aeroacoustic wave reflection on the fuselage surface (6th-16th BPF). Contour on surface shows the sound pressure level of the considered frequency range.

The influence of the fuselage components to the BVI radiation is shown in Figure 16 by the difference between the wavelet computed BVI signature of the aeroacoustic noise based on full helicopter and main rotor blade integration surface. The carpet is located 4.5 radii under the helicopter. Areas with no relevant BVI assignable noise (cf. Figure 13) are excluded from the comparison and coloured in grey. A highly increased area of the BVI related noise emission is found at the starboard side in front of the rotor. This area coincides with the previously computed reflection on the fuselage surface and shows a significant increase in the BVI signature compared to an aeroacoustic computation of the main rotor blades only. The opposite impact of the fuselage is found at the port side of the helicopter, where shading effects of the advancing blade side BVI reduce the BVI footprint in similar quantity.

A further BVI noise reduction area is found far downstream on the advancing blade side which results from tailboom shading of the retreating blade side BVI events.

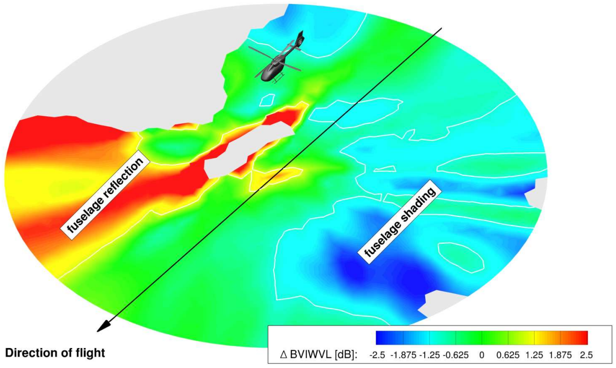

Fig. 16. Difference of BVI assignable noise 4.5 radii under the helicopter between full helicopter and blade integration surface (Grey areas excluded due to low overall noise level).

6.3 Aeroacoustic approach flight

To quantify the predictive capability of the numerical tool chain the computed aeroacoustic noise emission is compared to microphone data measured during the introduced approach test flight campaign.

Even if the high fidelity URANS computation includes the dominating aeroacoustic noise source (e.g. impulsive rotor noise, shear layers, engine exhaust, and low frequency detaching phenomena), high frequency broadband noise (e.g. trailing edge noise) and mechanical noise (e.g. engine noise) is not mapped in the current numerical tool. Therefore, an extraction of the impulsive main rotor and tail rotor tonal content from the measured signal is performed using the blade passing frequency information of both rotors. This signal is further denoted as MR+TR signal representing the impulsive noise sources, whereas the total signal is denoted as total. This means that the numerically computed signal level is expected to be between the impulsive noise MR+TR signal and the total signal.

The simulated data consists of 5 main rotor revolutions equal to a time window of $\approx 0.8\,\mathrm{s}$. To enable a comparison to the full approach flight, which lasts around 30 seconds, the data is assumed to be periodic and chained together to gain a database for the CAA computation over the required time window. As already described, the flow field is $\frac{1}{5}\,\mathrm{rev}$ periodic for the main noise emitting components, the main and tail rotor. The integration surface is moved according to the flight test trajectory over the microphone array which enables the consideration of the Doppler effect. The amplitude of the free-stream computed pressure time signal at the microphones is doubled to get a comparable signal to the ground plate (GP) microphone, representing the occurring total reflection of the pressure waves. According to the flight trajectory, the atmospheric damping of an undisturbed environment is taken into account.

Tone corrected Perceived Noise Level time histories (PNLT)

The comparison of the tone corrected Perceived Noise Level (PNLT) time histories for the three considered ground plate microphones is shown in Figure 17. The abscissa is centred around the fly-by time at 0 s (helicopter vertical over the center microphone), whereby negative values represent the approach and positive the departure flight phase. Besides the simulation result (blue), the PNLT data for the flight test - total (red) and MR+TR extracted signal (green) are shown. The shown solid flight test data is averaged over 5 approach flight signals and the minimum and maximum occurring PNLT levels are shown in the dashed lines.

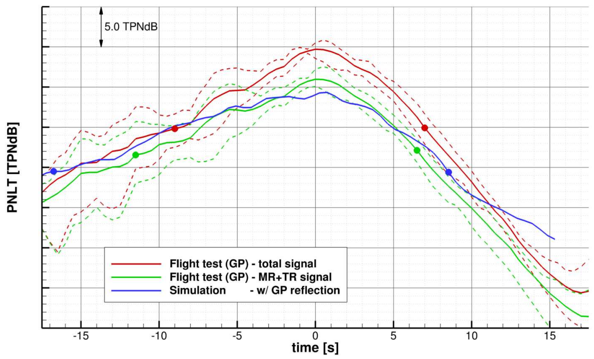

(a) Retreating blade side

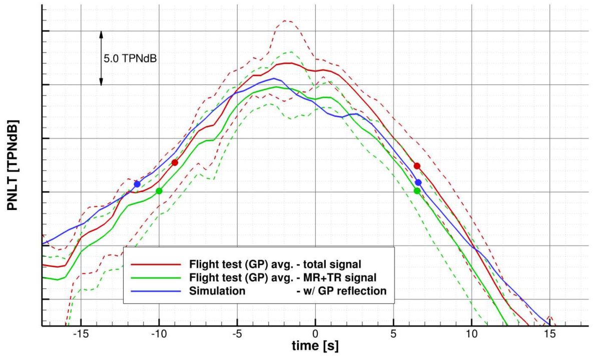

(b) Center

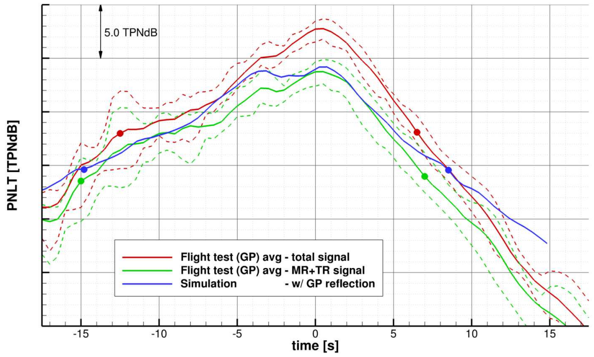

(c) Advancing blade side

Fig. 17. Comparison of PNLT time history of flight test microphones.

Comparing the flight test signal for all microphones during the approach it can be seen that this flight phase is mainly dominated by main rotor and tail rotor noise. At the fly-by position a higher difference between the flight test total and MR+TR signal is encountered, indicating higher proportions of non-rotor induced noise. Taking the simulated PNLT time histories into account, the approach phase and departure phase are captured very well with good accordance in the absolute PNTL value as well as the gradient. The slight deviation to the average PNTL flight test signals almost always stays within the flight test variations. The simulated values remain between the flight test MR+TR and total signal showing good accordance to the expected characteristic. Only particular deviations from the signals are found as in case at the fly-by time of the retreating blade side (cf. Figure 17(a)) and marginally at the center microphone (cf. Figure 17(a)).

At low level PNLT values, caused by large distance of the helicopter to the microphones, a slight flattening of the PNLT shape is found in case of the simulation (notable in cf. Figure 17(a) t$>$10 s). This results of the overall low noise level, where numerically caused background noise increases in proportion as well as longer noise transport through the atmosphere, which increases uncertainty in the tool chains atmospheric correction. The influence of the tail rotor to the PNLT values is notable in the flight test as well as in the simulation data. As seen in the tail rotor noise footprint in Figure 14(c), the noise is mainly produced sideways of the helicopter with higher noise emitted starboard, whereas nearly no noise is radiated directly below the helicopter. The same character is seen on the retreating and advancing blade sided microphone with peaks shortly after the fly-by position. As in the noise footprint, a higher influence at the advancing blade side microphone is present as well as no influence to the center microphone.

For the computation of the certification relevant Effective Perceived Noise Level (EPNL) value, a good accordance of the maximum PNLT value (PNLT$_{max}$) is requisite. Apart from the retreating blade side, the PNLT$_{max}$ values are in general captured with values between the TR+MR and the total signal. For the retreating blade side an underestimation of the maximum value of $>$0.5 TPNdB is present. Hence, the overall noise at this microphone is considerably lower compared to the other microphones, which increases the demand on the numerical tool chain additionally.

Further mandatory key values of PNLT time-history are the 10dB-down times, defining the integration boundaries for the computation of the EPNL value. Those are determined based on the PNLT$_{max}$ value and mark the time where initially and lastly the PNLT value exceed PNLT$_{max}$-10 TPNdB. The respective times are highlighted with dots in the PNLT time histories in Figure 17.

Due to the underestimation of the PNLT$_{max}$ value at the retreating blade side microphone, the 10 TPNdB-down times show higher deviation to the flight test. In the case of the other two microphones, the 10 TPNdB-down times are captured very well with only slight variation, since PNLT$_{max}$ as well as approach and departure gradients show good agreement with the flight test data.

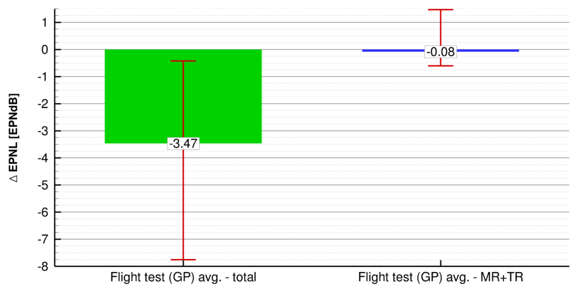

(a) Retreating blade side

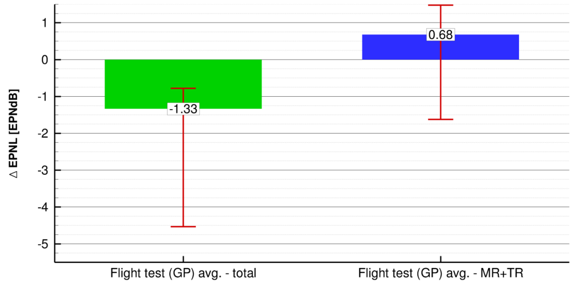

(b) Center

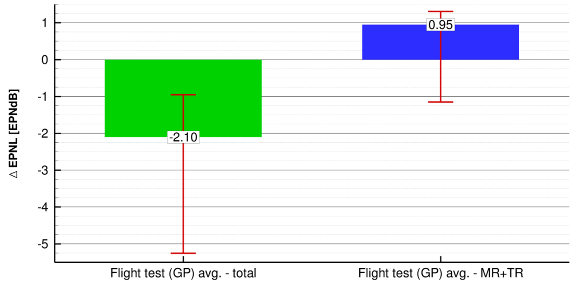

(c) Advancing blade side

Fig. 18. Comparison of full helicopter CAA-CFD computed ICAO approach flight EPNL values to total and MR+TR filtered experimental signal.

Effective Perceived Noise Level (EPNL)

The comparison of the EPNL value is shown in Figure 18 in terms of the deviation of the flight test average to the simulated results. The red bars indicate the respective deviation to the minimal and maximal occurring EPNL values of the considered flight cases. The simulation overestimates the MR+TR signal and underestimates the total signal in case of the center and advancing blade side microphone. This characteristic is attributed to the high fidelity URANS computation disregarding high frequency broadband noise and of course mechanical noise sources.

In case of the retreating blade side a general underestimation of the EPNL value is found with marginal difference to the MR+TR signal. In this case the PNLT time history explains the small deviation of the EPNL. The underestimation of the PNLT$_{max}$ value and the overestimation of the 10 TPNdB-down times cancel each other by integration. Therefore, the result is to be assessed carefully. At the other hand, the notably lower absolute EPNL value at this microphone constrains the relevance of its slight error for a global assessment of the result.

Pressure-time records

Besides the ICAO certification relevant values, sections of pressure time histories of the center microphone during the approach and fly-by time are shown in Figure 19. The flight test considered is picked out of the previously averaged flights. During the approach a very good agreement between the simulated and measured signal is present. The strength of the BVI events are captured as well as the basic noise, which is dominated by the main rotor frequency. Only a slight overestimation of the first BVI event is found. At the fly-by time spot, an excellent accordance can be found as well. The general magnitudes as well as the higher harmonic parts are clearly visible. A deviation of the simulation is present in an additional positive BVI caused pressure disturbance, which is missing in case of the flight test data. In the experimental data a slight positive peak, underestimated by the simulation, is present before the first common present BVI event occurs. However, this two events can not clearly be connected.

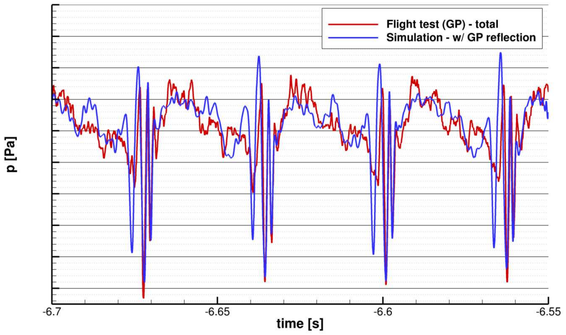

(a) Approach

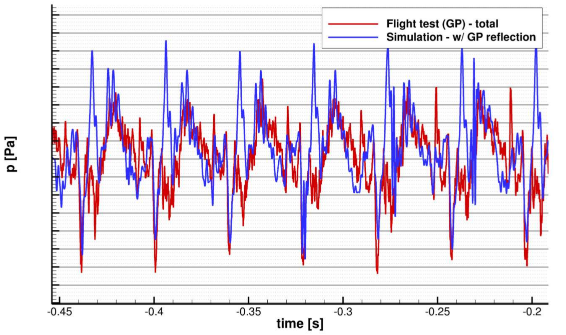

(b) Fly-by

Fig. 19. Comparison of the pressure time signals during approach and fly-by situation for the center microphone.

BVI proportion during approach flight

As a further comparison, the BVI share of the pressure time signal is determined and compared. Figure 20 shows the evaluation for the BVI dominated microphone at the center position. The dashed lines mark the total Sound Pressure Level (L) and the solid lines the BVI part detected by the wavelet filter.

As in the case of the PNLT time history, a very good accordance with the overall noise level is present. During the early approach and later departure phase a deviation between flight test and simulated BVI part is present. This is mainly caused by background noise in the flight test data, wherefore partially noise events could not be assigned clearly to BVI.

However, the previously illustrated BVI noise radiation character (cf. Figure 13) is also notable in the time history of the simulated microphone data, with two BVI peaks and a plateau at the fly-by position (-5 s<t<5 s). This characteristic is also found in the flight test data, where as in the case of the simulation, the approach peak directly before the fly-by situation shows the maximum BVI noise share. The short BVI noise reduction followed by another peak is in accordance with the simulation results. In the time phase around the fly-by time, the total BVI related noise shows good accordance in absolute value as well as relative to the total noise level.

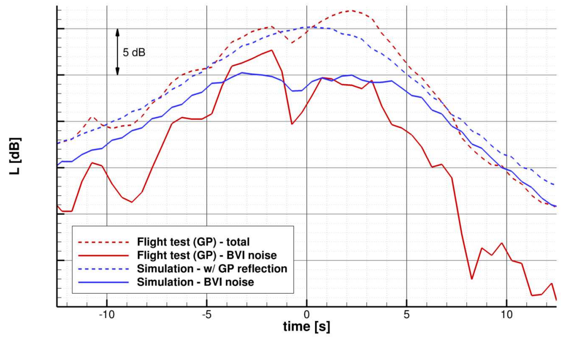

Fig. 20. Comparison of sound pressure level and BVI assigned noise proportion at the center microphone.

Comparison and assessment of earlier isolated rotor investigation

In the following, an assessment of the prior investigated isolated rotor is performed. The isolated rotor was computed with the same numerical tool chain and the same CFD mesh resolution. A detailed description of the investigation and its results including a comparison to the experimental data can be found in Reference 3.

Even if the results with ENPL deviation of around 3.5 dB to the flight test data were outstanding improvements compared to former aeroacoustic simulations, the next step to simulate the complete helicopter was a necessarily consequence to resolve the remaining offset.

The present evaluation of the full helicopter simulation revealed the influence of the helicopter components to the noise footprint in terms of shading and reflection effects. The overall noise emission was seen to reduce ($\sim$2 dB) due to the presence of the fuselage reflected by a lower PNLT value compared to the isolated rotor investigation.

Besides the influence of the geometry components, a slight difference (~1 dB) is introduced due to the trim strategy. The isolated rotor investigation was based on a 3 component trim. The trim objectives (thrust, pitch and roll moment) were pre-computed using low fidelity flight mechanic tools, since no flight test measurements for this quantities are available.

In case of the 6-DOF full helicopter trim, pre-computed trim objectives are obsolete. The approach enables the computation of a fully CFD based flight state determination, whereby the CFD shows high reliably computed loads. The remaining shortcomings are located in the dynamic blade model and CFD environmental settings (e.g. wind).

The results of this investigation campaign shows that reliable results for the complex aeroacoustic noise emission of a helicopter demands a high fidelity CFD computation in combination with the consideration of preferably every aeroacoustic influencing geometry component. However, it has to be noted that the isolated rotor simulation still gave reasonable results with a much lower simulation complexity (80 M vs. 190 M grid cells, 3-DOF vs. 6-DOF trim).

7 CONCLUSIONS

An assessment of the CFD-CSD-CAA based reproduction of helicopter noise emission in a BVI relevant descent flight phase is presented. Basis for the validation is given by a ICAO noise certification flight test campaign of the H145 helicopter.

In contrast to former simulations focusing on 3-DOF trimmed main rotors only, the current CFD simulation covers the complete helicopter geometry with a 6-DOF trim. Hereby, the influence of all helicopter components to the noise emission as well as the inclusion of noise sources beside the main rotor are considered.

Using a high resolution with 190 mio overall grid cells in combination with the 5th order WENO-Z method for the CFD computation ensures a detailed mapping of the noise generating phenomena, prominently BVI. The solution of the CFD flow field is forwarded to the CAA simulation to investigate the far field noise radiation.

The typical noise radiation character is found for the helicopter structure, and the BVI related noise could be assigned effectively using a wavelet filter for identification. The influence of the geometry components, especially the fuselage, could be resolved clearly with strong reflection and shading effects of the advancing blade side BVI events. Pursuing the effects, a influence of ±3 dB to BVI related noise is identified.

Investigating the approach flight noise of the helicopter shows very good accordance with the flight test data. The PNLT time histories are met in shape and absolute values within the flight test data variation. The followed certification relevant EPNL computation shows high accordance as well, where the numerical signal produces values between the flight test main rotor + tail rotor signal and the total signal. Taking the neglected high frequency broadband (URANS) and mechanical noise sources (e.g. engine noise) into account, this is the required range.

Compared to a previous isolated rotor investigation, the advantage of simulating the complete helicopter became evident. It was shown that with the component influences, the noise footprint of the helicopter changes partially considerably. As a result of this, the investigated flight test microphones changes in strength and shape reduce the deviation from flight test from 3.5 dB overestimation to less than 1.0 dB. This shows the necessity to consider the full helicopter geometry for high fidelity aeroacoustic noise emission results. The marginal deviations show the very good capability of the presented numerical tool chain to reflect the aeroacoustic characteristics of the helicopter in this complex flight state.

Next steps in investigating aeroacoustic helicopter flow fields will be the consideration of hybrid LES-URANS methods to include first broadband noise components.

The available high fidelity flow field constitutes an improvement of knowledge to industry. Based on those detailed investigations of the aeroacoustic influence, developments may further improve the aeroacoustic noise emission e.g. by absorbing surface materials on the fuselage to reduce constructive reflection. However, currently available computational resources in industry prohibit comparable simulations, thus this remains a task for research facilities in the near future.

ACKNOWLEDGEMENTS

This work was performed within the federal research project ECO-HC2, which is lead by Airbus Helicopter Deutschland GmbH.

The authors would like to thank Airbus Helicopters Deutschland GmbH for the esteemed cooperation within this project and beyond, as well as providing us experimental data to enable this investigation. We would like to express our thanks to the Federal Ministry of Economics and Technology for providing us the resources to realize this project. Furthermore, the investigation is based on the long-standing cooperation with the German Aerospace Center (DLR) making us their CFD code FLOWer available for advancements and research purpose, which we would like to thank for.

Further acknowledgement is made to the High Performance Computing Center in Stuttgart who provided us with support and service to perform the computations on their high performance computing system Hornet.

REFERENCES

[1] Boyd, D. D. J., “HART-II Acoustic Predictions using a Coupled CFD/CSD Method,” Proceedings of the American Helicopter Society, 65th Annual Forum, Grapevine, Texas, 2009.

[2] Ahmad, J. U. and Chaderjian, N. M., “High-Order Accurate CFD/CSD Simulation of the UH-60 Rotor in Forward Flight,” 29th AIAA Applied Aerodynamics Conference, Honolulu, Hawaii, 2011.

[3] Kowarsch, U., Lippert, D., Schneider, S., Keßler, M., and Krämer, E., “Aeroacoustic Simulation of an EC145T2 Rotor in descent flight,” 71th American Helicopter Society Annual Forum, Virginia Beach, VA, 2015.

[4] Kroll, N., Eisfeld, B., and Bleeke, H., “The Navier-Stokes code FLOWer,” *Notes on Numerical Fluid Mechanics*, 1999, pp. 58–71.

[5] Wilcox, D., “Multiscale Model for Turbulent Flows,” *AIAA Journal*, Vol. 26, No. 11, 1988, pp. 1311–1320.

[6] Jameson, A., “Time dependent calculations using multigrid, with applications to unsteady flows past airfoils and wings,” AIAA 10th Computational Fluid Dynamics Conference, Honolulu, HI, 1991.

[7] Eurocopter Deutschland GmbH, Internal Report, *Manual for the FLOWer HELI Version*, version 2008.1 rel 1012 edition, 2011.

[8] Kowarsch, U., Oehrle, C., Hollands, M., Keßler, M., and Krämer, E., *High Performance Computing in Science and Engineering 13*, Springer Verlag, 2013, Chapter Computation of Helicopter Phenomena Using a Higher Order Method, pp. 423–438.

[9] Kowarsch, U., Keßler, M., and Krämer, E., “High Order CFD-Simulation of the Rotor-Fuselage Interaction,” 39th European Rotorcraft Forum, Moscow, 2013.

[10] Kowarsch, U., Keßler, M., and Krämer, E., “CFD-Simulation of the Rotor Head Influence to the Rotor-Fuselage Interaction,” 40th European Rotorcraft Forum, Southampton, 2014.

[11] Borges, R., Carmona, M., Costa, B., and Don, W. S., “An improved weighted essentially non-oscillatory scheme for hyperbolic conservation laws,” *Journal of Computational Physics*, Vol. 227, (6), 2008, pp. 3191 – 3211.

[12] Toro, E. F., *Riemann Solvers and Numerical Methods for Fluid Dynamics*, Springer Verlag, Berlin, 1997.

[13] Johnson, W., *CAMRAD II Comprehensive analytical model of rotorcraft aerodynamics and dynamics*, fourth edition, 2009.

[14] Keßler, M. and Wagner, S., “Source-Time Dominant Aeroacoustics,” *Computers & Fluids*, Vol. 33, 2004, pp. 791–800.

[15] International Civil Aviation Organization, *Environmental Technical Manual - Volume I: Procedures for the Noise Certification of Aircraft*, doc. 9501 edition, 2012.

[16] Gareton, V., Gervais, M., and Heger, R., “Acoustic Design and Testing of the Eurocopter EC145T2 and EC175B - a harmonized Franco-German Approach,” 39th European Rotorcraft Forum, Moscow, 2013.

[17] Stephenson, J. and Greenwood, E., “Effects of Vehicle Weight and True Versus Indicated Airspeed on BVI Noise During Steady Descending Flight,” 71th American Helicopter Society Annual Forum, Virginia Beach, VA, 2015.